



Trans. Nonferrous Met. Soc. China 35(2025) 3323-3341

Transactions of Nonferrous Metals Society of China

www.tnmsc.cn



Compressive mechanical behavior and microstructure evolution of Ti-5.7Al-2.9Nb-1.8Fe-1.6Mo-1.5V-1Zr alloy under extreme conditions

Wen-fei PENG¹, Chao-qi DONG¹, Qiao-dong HUANG¹, Xiao-feng WANG^{1,2}, Oleksandr MOLIAR¹

- 1. Faculty of Mechanical Engineering and Mechanics, Ningbo University, Ningbo 315211, China;
- 2. Key Laboratory of Impact and Safety Engineering, Ministry of Education, Ningbo University, Ningbo 315211, China

Received 29 January 2024; accepted 30 October 2024

Abstract: Compressive mechanical behavior and microstructure evolution of Ti-5.7Al-2.9Nb-1.8Fe-1.6Mo-1.5V-1Zr alloy under extreme conditions were systematically investigated. The results show that strain rate and temperature have a significant influence on the mechanical behavior and microstructure. The alloy exhibits a positive strain rate sensitivity and negative temperature sensitivity under all temperature and strain rate conditions. The hotrolled alloy is composed of a bimodal structure including an equiaxed primary α_p phase and a transformed β phase. After compression deformation, the bimodal deformed structural features highly rely on the temperature and strain rate. At low temperature and room temperature, the volume fraction and size of α_p phase decrease with increasing temperature and strain rate. At high temperature, the volume fraction of the α phase is inversely correlated with temperature. A modified Johnson-Cook constitutive model is established, and the predicted results coincide well with the experimental results.

Key words: titanium alloy; extreme condition; mechanical behavior; microstructure; modified Johnson-Cook constitutive model

1 Introduction

 $\alpha+\beta$ titanium alloys have been widely used in aerospace, automobile manufacturing, biomedical and other fields due to their advantages of low density, high strength, excellent corrosion resistance, and good oxidation resistance [1–3]. Two phases, α and β , coexist in $\alpha+\beta$ titanium alloys, and their fractions, sizes and distributions mainly determine the mechanical properties of these alloys [4–6]. To further improve the mechanical properties of $\alpha+\beta$ titanium alloys, numerous researchers have carried out much work in alloy design and process optimization and have successfully understood the regulation of microstructure control [7–10].

In recent years, with the rapid development of

aerospace technology, people's exploration of the universe has entered a new stage. Engineering structures face extreme conditions in outer space; for example, spacecraft may face an ultralow temperature space environment, a high-temperature environment generated by airflow friction during the high-speed flight, and a high-strain rate environment generated by meteorite impact [11,12]. Therefore, new requirements have been proposed for the engineering materials. As an important aerospace material, $\alpha+\beta$ titanium alloys are necessary for obtaining an in-depth understanding of their mechanical behavior under various extreme conditions.

In the field of dynamic mechanics, several researchers have carried out related studies. ZHANG et al [13] investigated dynamic mechanical

behavior of a TC18 titanium alloy at room temperature using a split Hopkinson pressure bar (SHPB) device. The results showed that the flow stress behavior of TC18 titanium alloy exhibited strain rate sensitivity; the flow stress of the alloy increased significantly as the strain rate increased from 1033 to 5015 s⁻¹. ZHENG et al [14] studied the dynamic compression behavior of a TC4 titanium alloy at room temperature and reported that when the strain rate increased from 2000 to 3000 s⁻¹, the flow stress of the alloy increased by only 3.7%, indicating that the strain rate sensitivity was small.

In the field of high and low temperature research, the mechanical behaviors of $\alpha+\beta$ titanium alloys have also attracted widespread interest. LEI et al [15] studied the isothermal compressive deformation behavior of a TC11 titanium alloy in the temperature range of 1023-1373 K and reported that the flow stress of the alloy decreased with increasing temperature. Compared with that in the lower temperature region, the temperature sensitivity in the higher temperature region was lower. YU et al [16] studied the flow behavior and dynamic transformation of a TC17 titanium alloy through hot compression. The results revealed that the alloy possessed significant strain rate sensitivity and temperature sensitivity at high temperatures; the flow stress decreased significantly with increasing deformation temperature and decreasing strain rate. LEE et al [17] studied the compressive mechanical behavior of a TC4 titanium alloy at 123, 273 and 298 K. The results showed that as the temperature increased, the flow stress, work hardening rate, and temperature sensitivity decreased. The results of other studies on the low-temperature mechanical behavior of TC4 titanium alloys also support this conclusion [18,19]. WANG et al [20] investigated the mechanical behavior of Ti-5Al-1V-1Sn-1Zr-0.8Mo (Ti5111) alloy in the temperature range of 77-273 K. They found that the alloy had significant temperature sensitivity at low temperatures and the flow stress increased significantly.

At present, studies on the mechanical behavior of $\alpha+\beta$ titanium alloys under extreme conditions have focused mainly on a single strain rate or single temperature, but few studies have focused on the coupling effect within a wide strain rate and wide temperature range. In addition, the conventional

research objects are commercial $\alpha+\beta$ titanium alloys, such as TC4, TC11 and TC17. Therefore, a new $\alpha+\beta$ titanium alloy (Ti-5.7Al-2.9Nb-1.8Fe-1.6Mo-1.5V-1Zr) was selected for the present study. Compared with TC4 titanium alloy, this alloy contains additional and greater amounts of β -stabilizing elements, Fe, Nb, Zr, and Mo; thus, it possesses a lower phase transition point and greater strength and toughness. This work systematically investigated the mechanical behavior and microstructure evolution of the alloy under extreme conditions. and a constitutive model established. The objective is to understand the mechanical response and constitutive behavior of titanium alloys under extreme conditions and hopefully promote their engineering applications.

2 Experimental

2.1 Materials preparation

The starting material was a cast $\alpha + \beta$ titanium Ti-5.7Al-2.9Nb-1.8Fe-1.6Mo-1.5V-1Zr alloy, (wt.%), fabricated in a consumable electrode melting furnace, and the chemical composition is given in Table 1. The cast ingot was cut into several bars with a diameter of 16 mm and hot rolled with three passes on a four-high rolling mill to achieve a final diameter of 12 mm. To ensure the quality of the hot rolling process, the initial rolling temperature was controlled at 1200 K, and the finishing rolling temperature was 1000 K ($\alpha + \beta \Longrightarrow$ β) transformation temperature is approximately (1164±3) K. In addition, an intermediate annealing treatment at 1063 K for 1 h between rolling passes was adopted for the hot rolled bars. A process flow diagram of Ti-5.7Al-2.9Nb-1.8Fe-1.6 Mo-1.5V-1Zr alloy is clearly revealed in Fig. 1.

Table 1 Chemical composition of Ti-5.7Al-2.9Nb-1.8Fe-1.6 Mo-1.5V-1Zr alloy (wt.%)

Al	Fe	Mo	Nb	V	Zr
5.68	1.81	1.58	2.90	1.48	0.92
С	Н	О		N	Ti
0.008	0.001	0.09	5	0.006	Bal.

2.2 Mechanical behavior characterization

Low strain rate compression tests (0.002, 0.01, 0.02 and 0.05 $s^{-1})$ at low temperature (203 and 233 K) and room temperature (293 K) were

performed on a SUST CMT7106NB universal testing machine equipped with an environmental chamber. A low temperature environment was achieved by vaporization and liquefaction of the refrigerant in the compressor. Low strain rate (0.01, 0.1 and 1 s⁻¹) compression tests at high temperature (973, 1073 and 1173 K) were conducted on an MMS-100 thermal simulator. The dynamic compression tests (1500, 2000, 2500 s⁻¹) at room temperature were performed using a split Hopkinson pressure bar (SHPB). A schematic illustration of the SHPB device is shown in Fig. 2. The specimens were pasted between the incident bar and the transmitted bar using Vaseline. Loading was applied along the axial direction of the specimen, and the strain sensors fixed on the incident bar and the transmitted bar (strain gauge) recorded the pulse signals of the incident wave, reflected wave, and transmitted wave during the experiment. Based on the 1D elastic wave theory [21], the pulse was subsequently analyzed to determine the stress, strain rate and strain. For the low and room temperature compression tests, cylindrical specimens with dimensions of d5 mm × 5 mm were prepared; for the high temperature compression test, cylindrical specimens with dimensions of $d10 \text{ mm} \times 15 \text{ mm}$ were prepared. To ensure the reliability of the results, all the compression tests were repeated three times.

To investigate the compressive mechanical behavior of the alloy under different experimental conditions, it is essential to analyze the true stress–strain curves of the alloy. The relationships among the engineering stress (σ_e), true stress (σ_T), engineering strain (σ_e), and true strain (σ_T) can be expressed by the following expressions:

$$\sigma_{\mathrm{T}} = \sigma_{\mathrm{e}}(1 + \varepsilon_{\mathrm{e}}) \tag{1}$$

$$\varepsilon_{\mathrm{T}} = \ln(1 + \varepsilon_{\mathrm{e}})$$
 (2)

2.3 Microstructure characterization

The microstructure and fracture morphology of the specimens were observed using a Carl Zeiss Axio Imager A2m metallographic microscope (OM) and a Hitachi SU5000 scanning electron microscope (SEM). Figure 3 shows the observation surfaces for different specimens. The specimen preparation steps for OM and SEM observations were as follows. The specimens were roughly ground with 500 grit sandpaper first and then finely ground sequentially with 1000, 1500, 2000 and 4000 grit sandpaper; after that, they were mechanically polished with polishing paste (2.5 and 1 µm), and they were finally etched by a Kroll etchant (5 vol.% HF, 15 vol.% HNO3 and 80 vol.% H₂O). Electron backscatter diffraction (EBSD) was used to analyze the microstructure of the hot-rolled titanium alloy. For the EBSD characterization, the acceleration voltage was 20 kV, the working distance was 10 mm, the tilt angle of the specimen stage was 70°, and the scanning step size was set as 0.025 µm. To acquire the inverse pole figure map

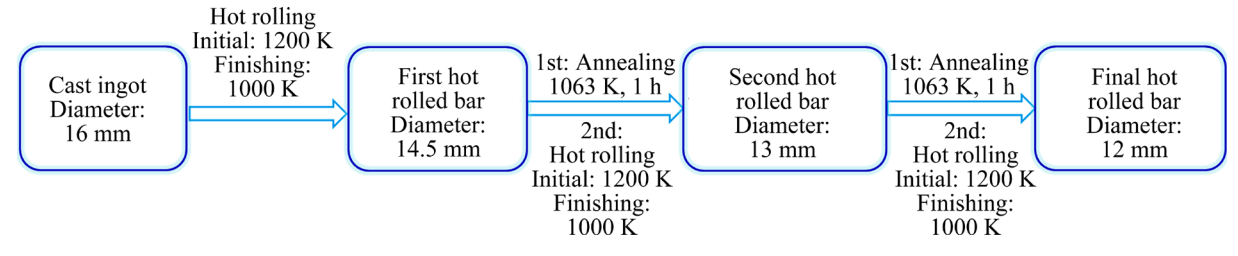


Fig. 1 Process flow diagram of Ti-5.7Al-2.9Nb-1.8Fe-1.6 Mo-1.5V-1Zr alloy

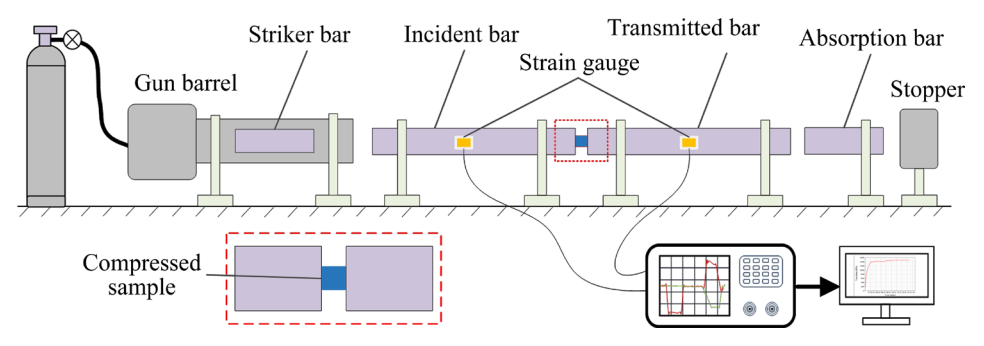


Fig. 2 Schematic illustration of split Hopkinson compression bar device

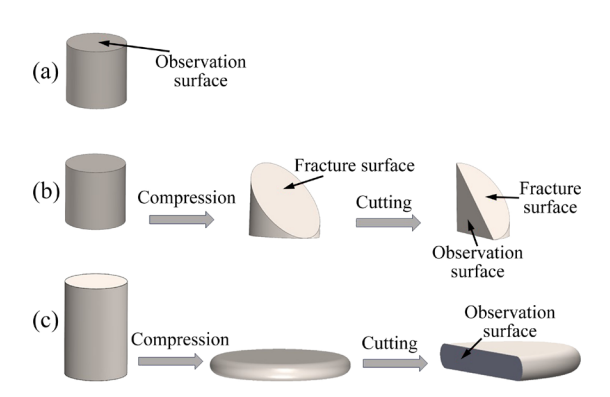


Fig. 3 Schematic diagram showing microscopic characterization surface: (a) Hot rolled titanium alloy; (b) Fractured specimens subjected to low and room temperature deformation; (c) Deformation specimens subjected to high temperature deformation

and phase distribution map, Channel 5 software was used for post-processing. EBSD specimens were prepared by grinding, mechanical polishing, and finally electro-polishing (60 mL perchloric acid + 590 mL methanol).

3 Results and discussion

3.1 Mechanical behavior

Figure 4 shows the true plastic stress-strain curves of the Ti-5.7Al-2.9Nb-1.8Fe-1.6Mo-1.5V-1Zr alloy at different temperatures over a wide range of strain rates. The different flow characteristics for those curves under a specific temperature condition imply that the alloy exhibits different plastic mechanical behaviors. To be more explicit, the alloy possesses strain rate sensitivity. Figures 4(a-c) depict the plastic mechanical behaviors of the alloy at room temperature and low temperature. When the strain rate is in the range of 0.002-0.05 s⁻¹, the trends of the true plastic stressstrain curves are relatively close: the flow stress increases slowly in the early plastic deformation stage, reaches the peak stress value, and then decreases slowly until fracture occurs. As the strain rate increases, the flow stress changes slightly. Under strain rate conditions of 1500–2500 s⁻¹, there is a significant fluctuation in the flow stress, and there is a slight change in the flow stress with increasing strain rate; however, when the strain rate increases from the low strain rate region $(0.002-0.05 \text{ s}^{-1})$ to the high strain rate region $(1500-2500 \text{ s}^{-1}),$ the flow stress increases

significantly. Figures 4(d-f) show the true plastic curves at high temperatures (973–1173 K). All the curves exhibit a similar trend in which the flow stress decreases continuously until a predefined deformation of 0.7 is reached. Under high temperature conditions, the flow stress increases significantly as the strain rate increases. Additionally, no fracture occurs in the alloy even when the deformation reaches 0.7. This is mainly because the diffusion and slip mechanisms inside the alloy are more active at higher temperatures, increasing the deformation ability of the alloy even at a high strain rate.

The strain rate sensitivity coefficient (m) is an important parameter for quantitatively describing the dependence of the flow stress on the strain rate, and its expression is as follows [22,23]:

$$m = \left(\frac{\partial \ln \sigma}{\partial \ln \dot{\varepsilon}}\right)_{\varepsilon, T} \tag{3}$$

where σ is the true stress, $\dot{\varepsilon}$ is the strain rate, m is the strain rate sensitivity coefficient, and ε and T are the true strain and temperature under the given conditions, respectively.

The m value of the alloy can be acquired through the logarithmic plots of true stress (σ) versus $\dot{\varepsilon}$ at a given true strain of 0.3, as presented in Fig. 5. The m values are different for different temperatures, and are somewhat dependent on the strain rate. At 203, 233 and 293 K, the m values under the low strain rate conditions (0.002–0.05 s⁻¹) are very low, and they are 0.0157, 0.0186 and 0.0111, respectively (Fig. 5(a)). At 293 K, unlike the m value under low strain rate conditions, the m value under high strain rate conditions of $1500-2500 \text{ s}^{-1}$ increases to 0.0444 (Fig. 5(b)). Unlike those at low and room temperatures, the alloys at higher temperatures of 973, 1073 and 1173 K and strain rate of 0.01-1 s⁻¹ exhibit higher m values, and they are 0.184, 0.238 and 0.249, respectively (Fig. 5(c)). According to Fig. 5(d), the strain rate sensitivity of the alloy is greater at high temperature than at room and low temperatures.

Figure 6 shows the true plastic mechanical behaviors of the alloy under different strain rate conditions over a wide temperature range. Clearly, under special strain rate conditions, all the curves reveal different flow characteristics, reflecting that the alloy possesses temperature sensitivity. From Figs. 6(a-d), under a special strain rate condition

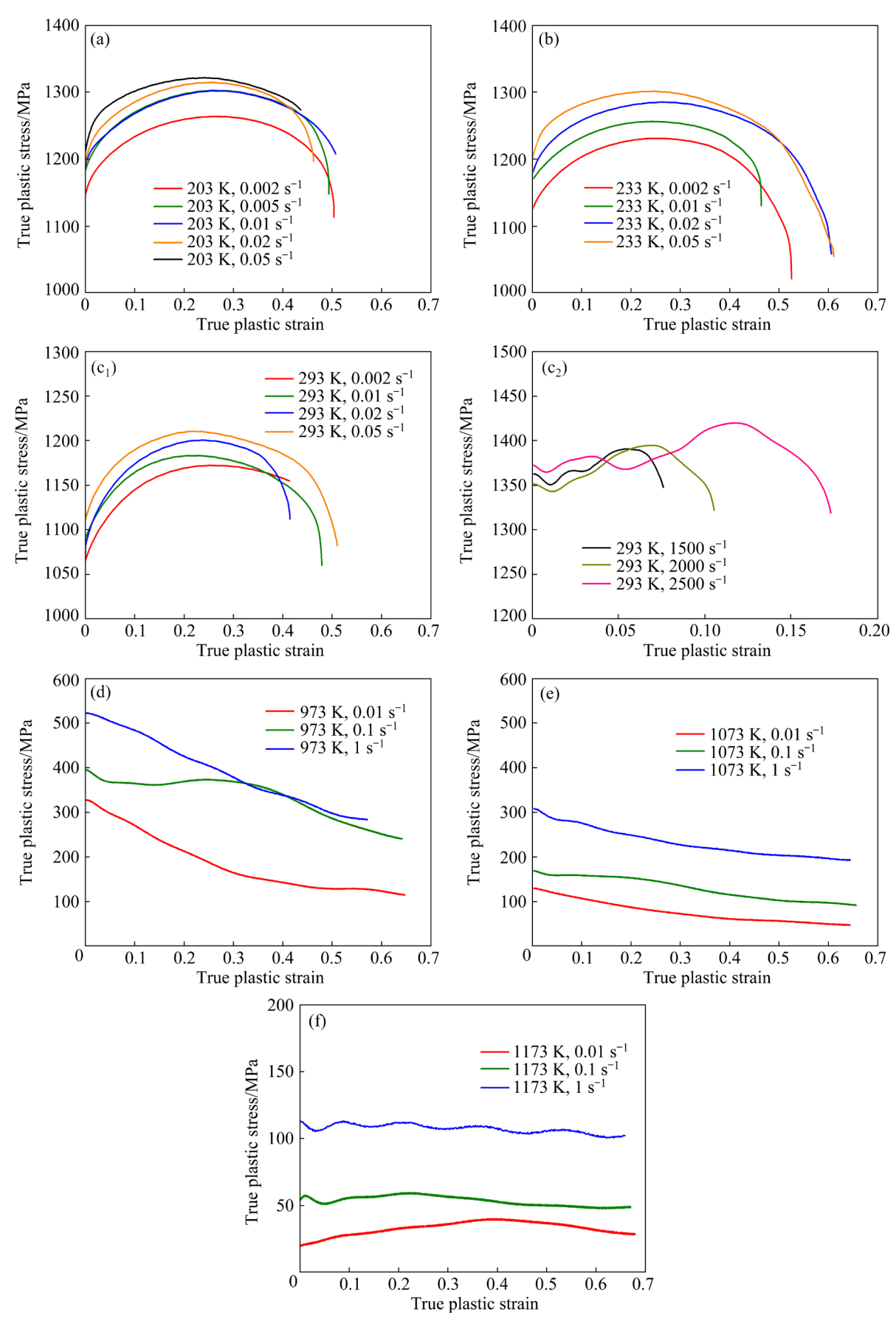


Fig. 4 True plastic stress–strain curves of titanium alloy at different temperatures: (a) 203 K; (b) 233 K; (c_1 , c_2) 293 K; (d) 973 K; (e) 1073 K; (f) 1173 K

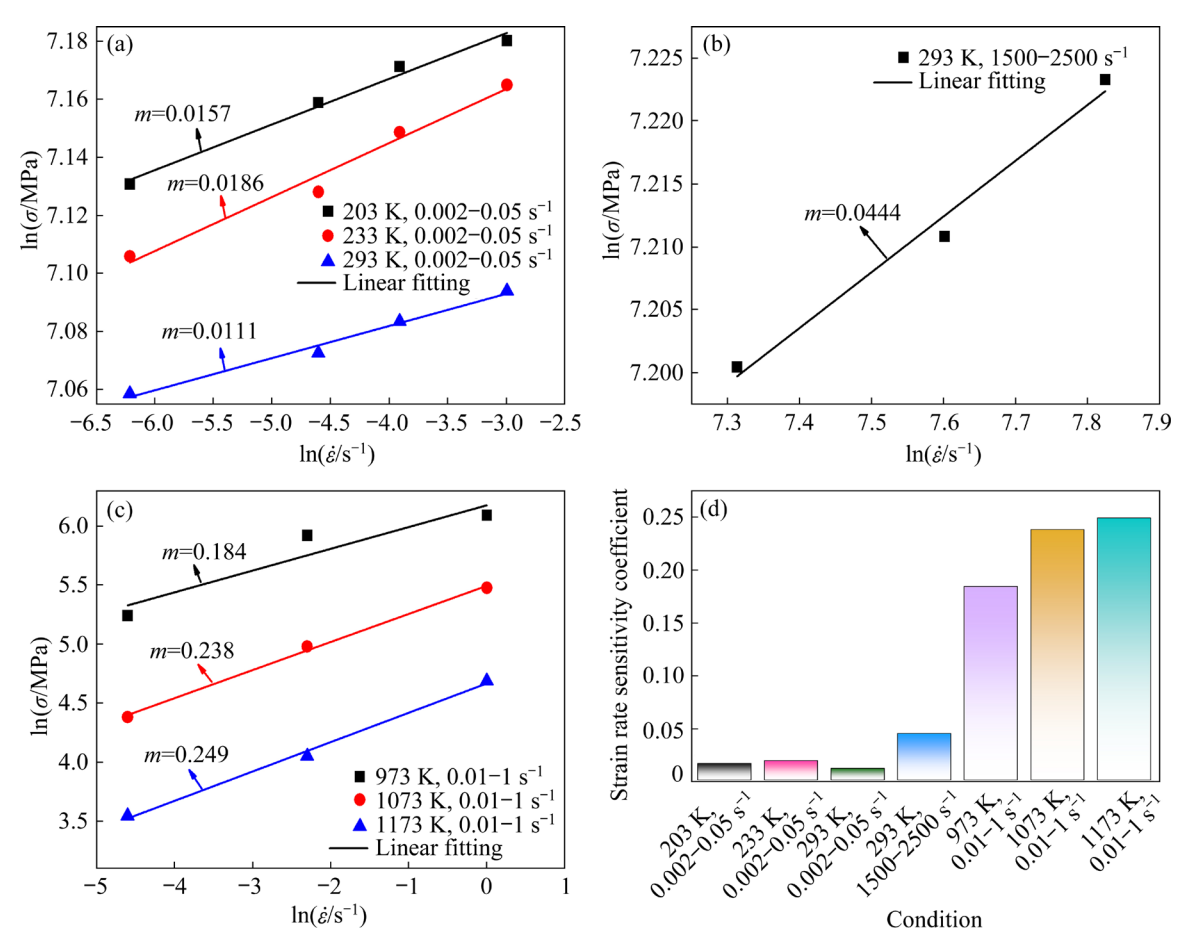


Fig. 5 Strain rate sensitivity coefficient (m) of titanium alloy under different temperature conditions: (a) Low and room temperature, and low strain rate; (b) Room temperature, and high strain rate; (c) High temperature, and low strain rate; (d) Comparison of m value

(0.002-0.05 s⁻¹), the trends of the stress-strain curves are relatively similar for temperatures ranging from 203 to 293 K that the flow stress increases slowly to an extreme value at first and then decreases slowly. Notably, the flow stress of the alloy decreases significantly with increasing temperature, implying that low temperature is beneficial for enhancing strength than room temperature. This phenomenon can be mainly attributed to two facts [24,25]. First, since dislocation movement is closely related to thermal-activated process, a decrease in temperature may result in a decreased possibility of dislocations movement; thus, additional stress is needed for dislocations to overcome the obstacles. Second, low temperature deformation can develop a higher density of dislocations and twinning; thus, a higher stress is also needed for the movement of dislocations. Under a special strain rate condition (0.01–1 s⁻¹), the trends of the stress–strain curves are also similar for a high temperature range of 973–1173 K (Figs. 6(b, e, f)), in which the flow stress decreases with increasing true strain. In addition, the flow stress in the alloy decreases significantly with increasing temperature.

To quantitatively describe the effect of deformation temperature on flow stress, the temperature sensitivity index is a very useful parameter and can be expressed as follows [26]:

$$q = \left(\frac{\partial \ln \sigma}{\partial \ln T}\right)_{\varepsilon,\dot{\varepsilon}} \tag{4}$$

According to Eq. (4) and Fig. 6, the q values can be obtained through data fitting of logarithmic plots of true stress versus logarithmic plots of temperature at the given true strain of 0.3, as revealed in Fig. 7. The alloy possesses different q values under different strain rate conditions. At strain rates of 0.002, 0.01, 0.02 and 0.05 s⁻¹, the q values at low and room temperatures (203–293 K) are -0.198, -0.236, -0.243, and -0.243, respectively (Fig. 7(a)). At strain rate of 0.01, 0.1

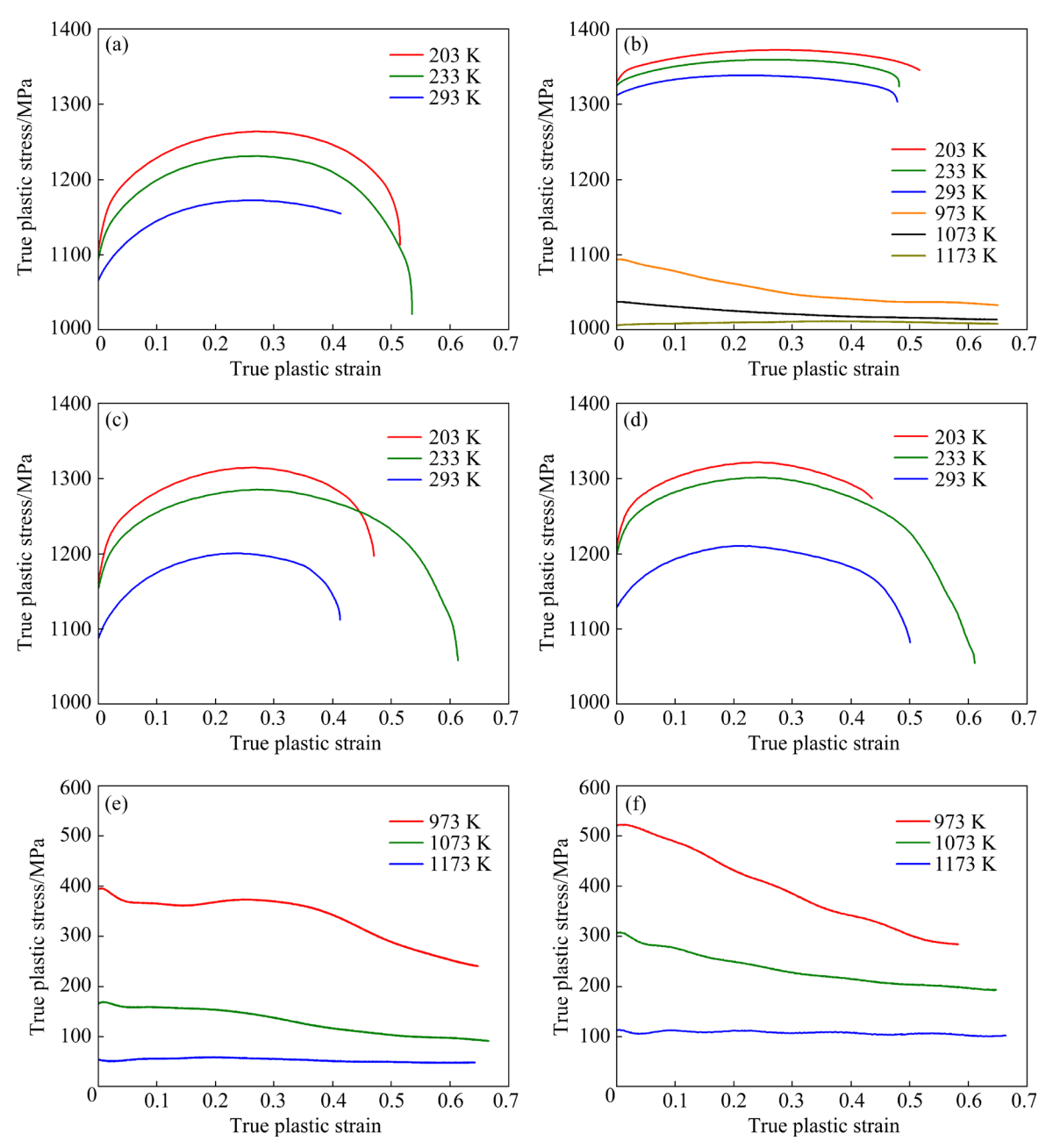


Fig. 6 True plastic stress–strain curves of titanium alloy under different strain rate conditions: (a) 0.002 s^{-1} ; (b) 0.01 s^{-1} ; (c) 0.02 s^{-1} ; (d) 0.05 s^{-1} ; (e) 0.1 s^{-1} ; (f) 1 s^{-1}

and $1 \, \mathrm{s}^{-1}$, the q values at room and high temperatures (973–1173 K) are much lower, and they are -9.04, -9.98 and -7.46, respectively (Fig. 7(b)). Since the calculated temperature sensitivity indices are all negative values, their absolute values can also reflect the temperature sensitivity well. Figure 7(c) compares the absolute q values under different conditions. It can be found that the temperature sensitivity at 973–1173 K is much greater than that at 203–293 K under the same strain rate conditions. The main reason is that dynamic recrystallization occurs more

easily with increasing temperature and continuous accumulation of dislocations, thus exacerbating the thermal softening behavior of the alloy. Overall, the alloy possesses a higher temperature sensitivity under high temperature conditions.

To further investigate the effects of temperature and strain rate on the work hardening effect of alloys, it is necessary to calculate the work hardening rate (θ) for a quantitative description, and the expression is as follows [22]:

$$\theta = d\sigma/d\varepsilon$$
 (5)

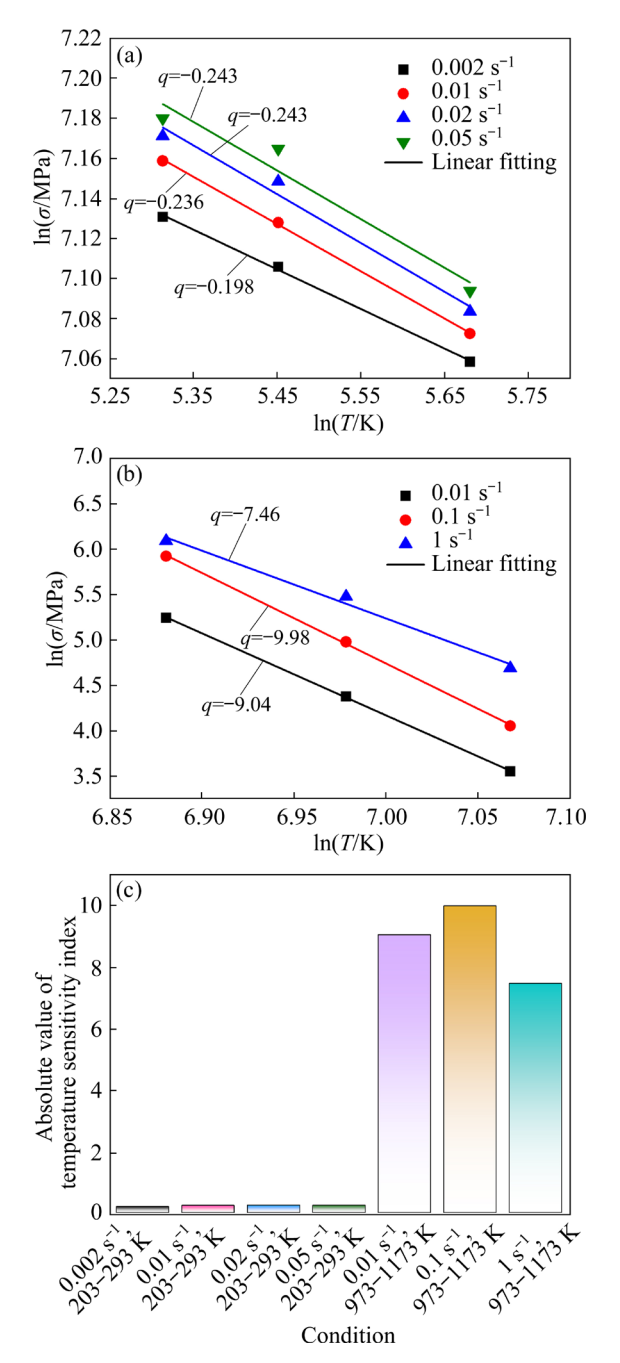


Fig. 7 Temperature sensitivity index (q) of titanium alloy at different strain rates: (a) At 203–293 K; (b) At 973–1173 K; (c) Comparison of absolute q value

Due to the thermal softening behavior of the alloy at high temperature, only the work hardening rate under low and room temperature conditions was analyzed. Figure 8 shows the true plastic strain—work hardening rate curves of the alloy under different conditions. Under low strain rate conditions, the work hardening rate curves at 203 and 293 K exhibit similar characteristics, and the curves can be divided into two stages: the work

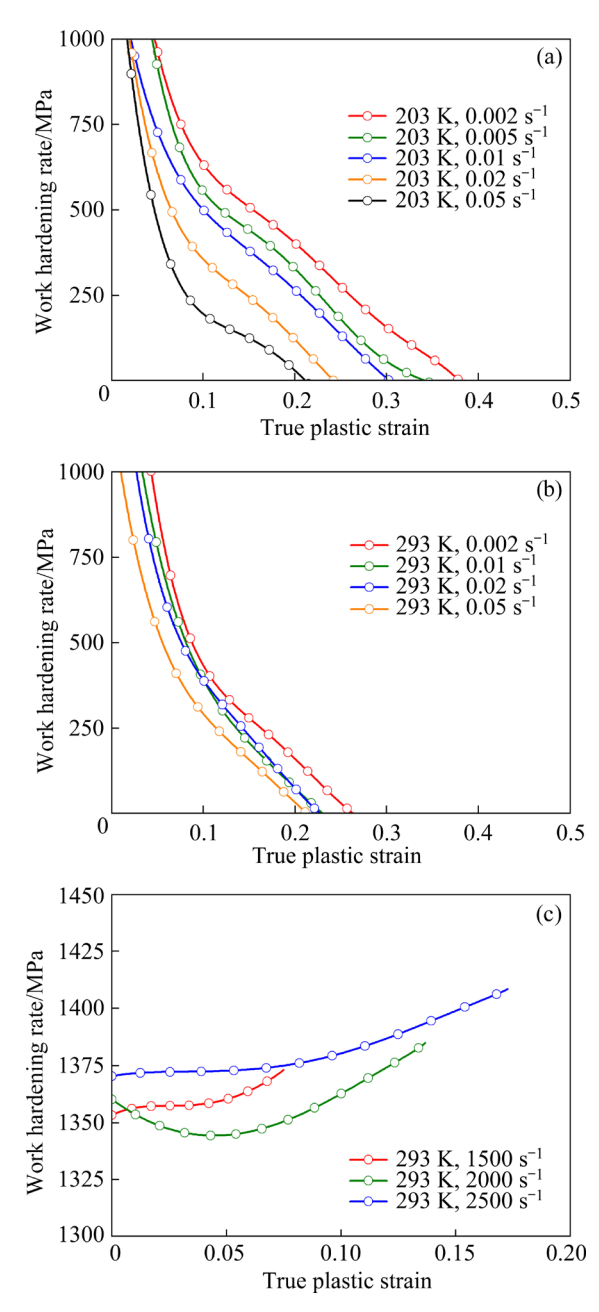


Fig. 8 True plastic strain—work hardening rate curves of titanium alloy under different conditions: (a) 203 K and low strain rate; (b) 293 K and low strain rate; (c) 293 K and high strain rate

hardening rate decreases sharply first, and then decreases slowly. Under high strain rate conditions, the work hardening curve at 293 K tends to be horizontal. In addition, compared with the low strain rate condition, the high strain rate condition corresponds to a higher work hardening rate. Notably, compared to that at room temperature, the effect of the strain rate on the work hardening rate is more significant at low temperatures. This is because dislocation generation and proliferation are

closely related to temperature, and a decrease in temperature increases the resistance to dislocation movement inside a material; thus, the strain rate can significantly influence the work hardening rate.

The above results show that the mechanical behaviors of the alloy under different extreme conditions are different; thus, the fracture characteristics may also be different. It is necessary to observe the related fracture morphology. In this study, since only the specimens compressed at low temperature and room temperature fractured,

four typical specimens under different conditions, namely, (203 K, $0.002~s^{-1}$), (233 K, $0.002~s^{-1}$), (293 K, $0.002~s^{-1}$) and (293 K, $2000~s^{-1}$), were selected for analyzing.

3.2 Fracture morphology

Figure 9 shows the compression fracture morphology of the specimens. Macroscopically, they exhibit the same shear fracture mode, and all the fracture surfaces are oriented by 45° with respect to the compression direction. Micro-

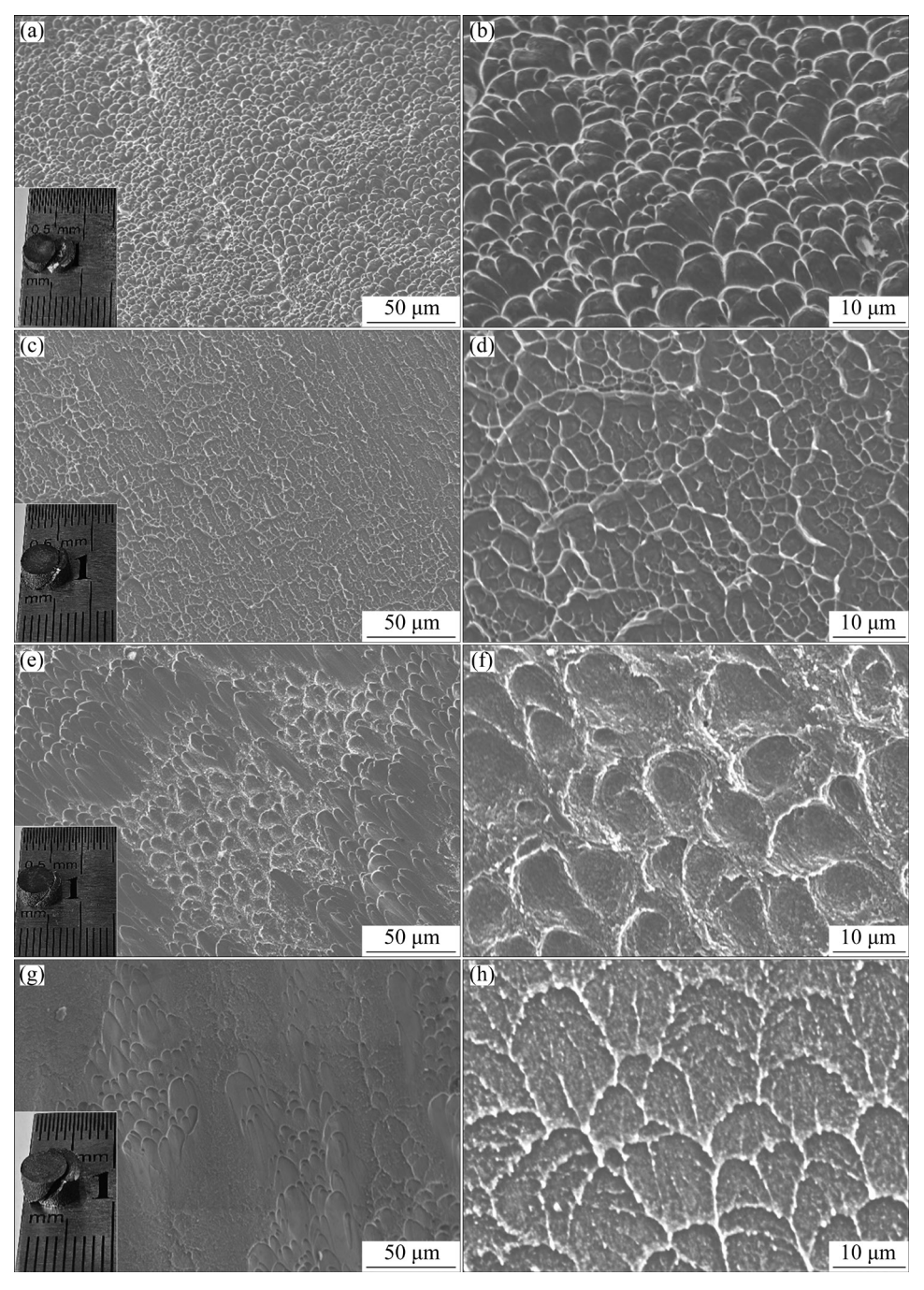


Fig. 9 Fracture morphologies of titanium alloy under different conditions: (a, b) 203 K, $0.002 \, s^{-1}$; (c, d) 233 K, $0.002 \, s^{-1}$; (e, f) 293 K, $0.002 \, s^{-1}$; (g, h) 293 K, $2000 \, s^{-1}$

scopically, under a low strain rate condition of 0.002 s⁻¹, the temperature significantly affects the fracture morphology of those specimens. At 203 K, the fracture morphology exhibits a typical brittle fracture, characterized by a smooth fracture surface. Moreover, a continuous, semicircular "fish scale" layered structure appears on cross-section, as revealed in Figs. 9(a, b). The arrangement of these "fish scale" structures is consistent with the direction of fracture progression, and the formation of a "fish-scale fracture" is related to the microscopic style of crack propagation. When a crack propagates according to a special grain direction or layered structure, a fish-scale fracture can be generated. At 233 K, many dimples appear on the fractured surface, indicating that the alloy changes from brittle fracture to ductile fracture. This transition is due to the increase in plasticity with increasing temperature (Figs. 9(c, d)). As the temperature further increases, the fracture morphology exhibits relatively deep dimples at 293 K (Figs. 9(e, f)), which indicates enhanced plastic flow and ductile fracture characteristics. At high strain rate of $2000\ s^{-1}$, a large flat and smooth area and a small amount of ductile dimples appear on the fractured surface, indicating that the alloy undergoes brittle-ductile mixed fracture. Notably, the flat and smooth fracture surface is due mainly to the very short time required for the alloy to undergo shear failure, and ductile dimples at the failure front can be developed only along the nearest failure direction.

3.3 Microstructure

Figure 10 shows the microstructure of the hot rolled titanium alloy. According to the OM and SEM images (Figs. 10(a, b)), the alloy is composed of a typical bimodal microstructure, including an equiaxed primary α_p phase and a transformed β phase. The transformed β phase includes the residual β phase and acicular secondary α_s phase. The phase distribution is highly important for determining the mechanical properties. According to the statistics, the volume fraction and the equivalent diameter of equiaxed α_p phase are 39% and 2.3 µm, respectively; the volume fraction of the secondary α_s phase is 23%. From Fig. 10(c), the volume fraction of α phase with a hexagonal close-packed crystal structure (HCP) is 64%.

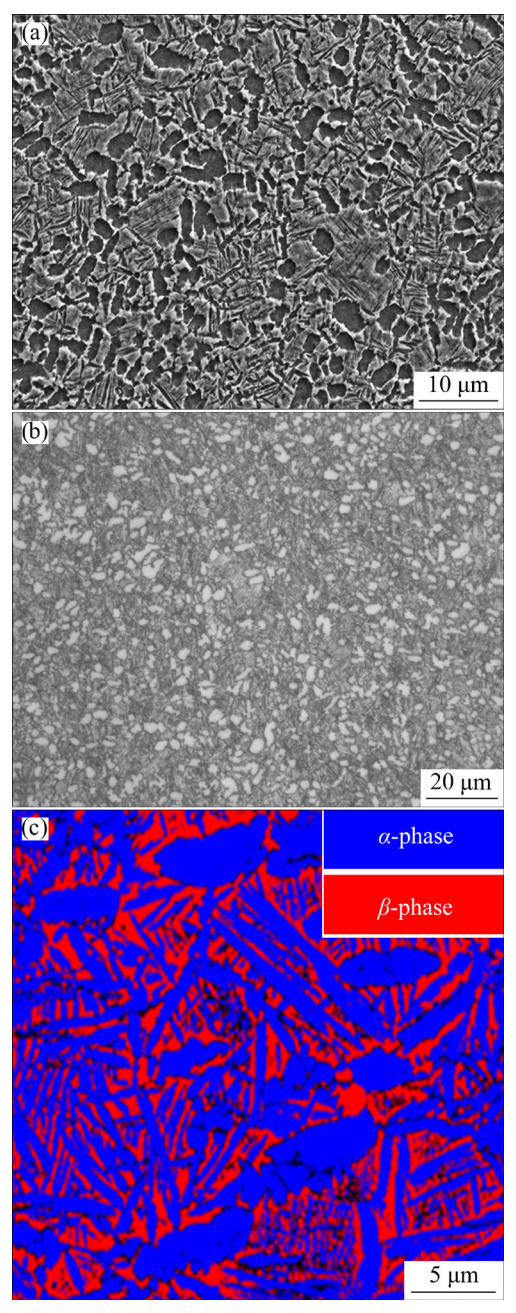


Fig. 10 Hot rolling microstructure of titanium alloy: (a) SEM image; (b) OM image; (c) Phase distribution map

After compression tests, the microstructure may undergo changes. Figure 11 reveals the deformation microstructure in vicinities of the fracture regions of the specimens at different temperatures and strain rates. It can be found that the alloy is still composed of a bimodal microstructure. Compared with the initial microstructure, the original primary α_p phase transforms from equiaxed grains to elongated grains, indicating that the deformation has a significant influence on grain shape. In addition, significant differences are

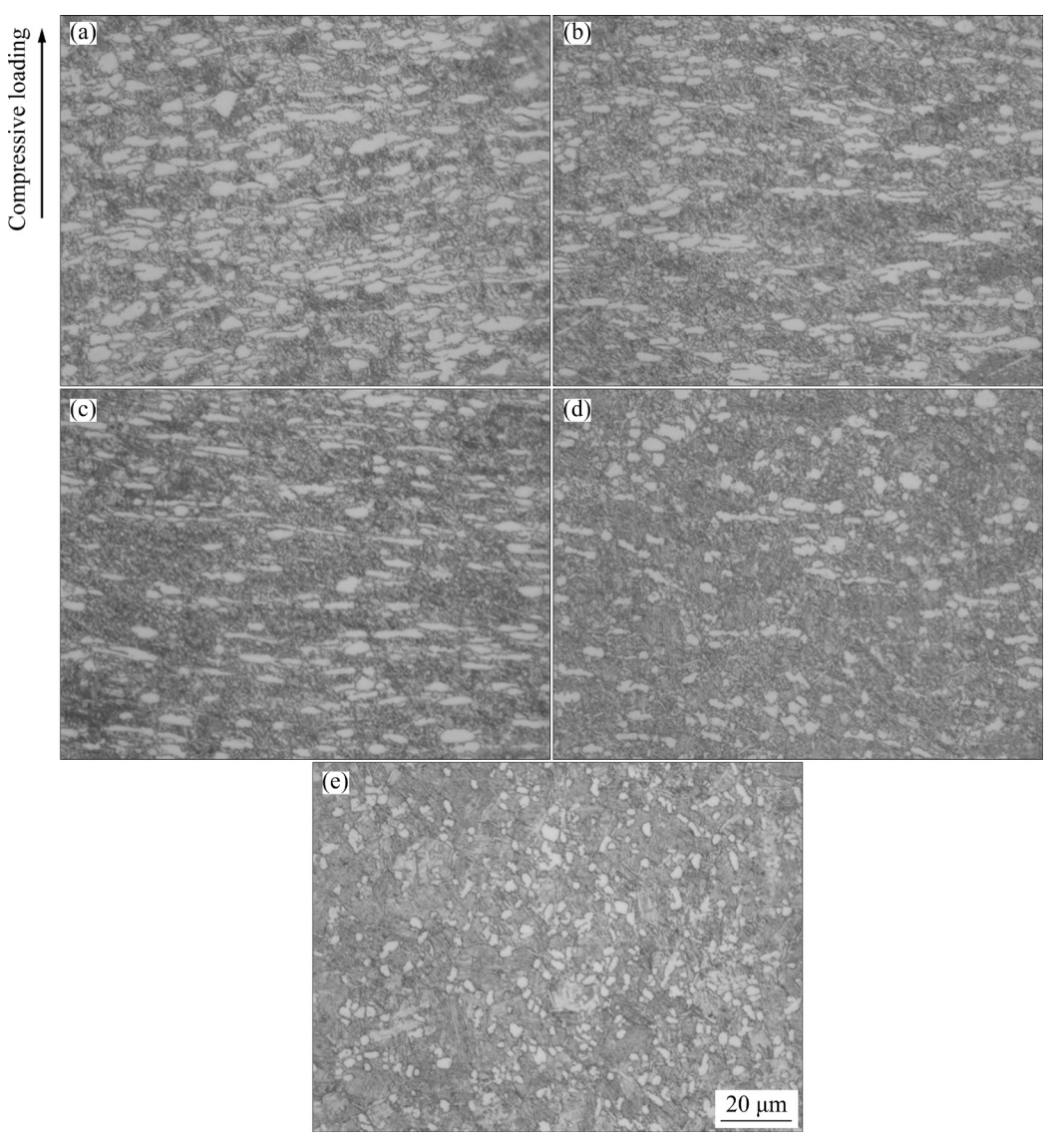


Fig. 11 Microstructure in vicinities of fracture regions of compressed specimens at different temperatures and strain rates: (a) 203 K, $0.002 \, \text{s}^{-1}$; (b) 203 K, $0.01 \, \text{s}^{-1}$; (c) 293 K, $0.002 \, \text{s}^{-1}$; (d) 293 K, $0.01 \, \text{s}^{-1}$; (e) 293 K, $0.003 \, \text{s}^{-1}$

observed in the quantity and morphology of the α_p phase at different temperatures and strain rates.

Further microstructure details are presented in Fig. 12. The morphologies and distributions of the α_p and α_s phases for those deformed specimens are significantly different. According to the statistical calculations, the volume fraction and equivalent size of the α_p phase gradually increase with decreasing temperature and strain rate. This is caused by the stress-induced phase transformation of titanium alloy. It has been documented [27] that when a $\alpha+\beta$ titanium alloy is subjected to stress, the β phase (BCC) in the alloy transforms into the α' phase (HCP). Under conditions of low temperature and low strain rate, the material deforms slowly, which leads to a uniform distribution of local

strains and local stresses inside the grains, and the local region near the grain boundary is more likely to satisfy the stress and deformation conditions required for phase transformation, which gives the newly formed α' martensite more time to transform into the coarse equiaxed α phase [28,29]. Secondary α_s phase is also significantly influenced by the strain rate and temperature. As the temperature increases, the length of the secondary α_s phase gradually decreases and its width gradually increases; as the strain rate increases from 0.01 to $2000 \,\mathrm{s}^{-1}$, the length of the secondary $\alpha_{\rm s}$ phase approximately doubles, and the width decreases half. Specifically, at a low strain rate of 0.01 s⁻¹, a large amount of uniformly distributed and fine acicular secondary α_s phases appear at 203 and

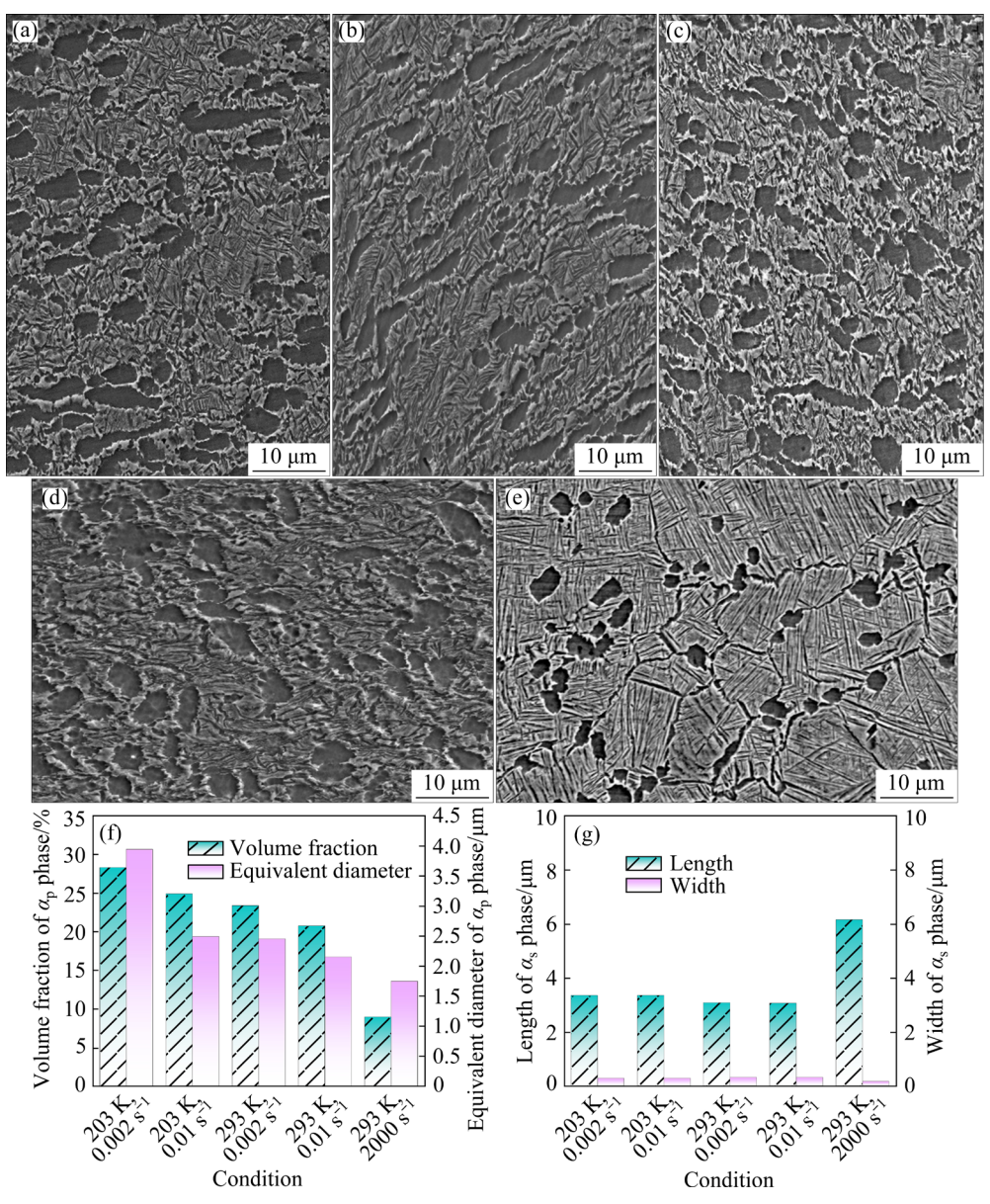


Fig. 12 Phase distribution in vicinities of fracture regions of compressed specimens at different temperatures and strain rates of (203 K, 0.002 s⁻¹) (a), (203 K, 0.01 s⁻¹) (b), (293 K, 0.002 s⁻¹) (c), (293 K, 0.01 s⁻¹) (d) and (293 K, 2000 s⁻¹) (e); Statistics of α_p (f) and α_s (g) phases

293 K, and their average aspect ratios are 12:1 and 10:1, respectively. This observation can be ascribed to the following fact. At low temperature, the slip system for the secondary α_s phase of the HCP structure is relatively limited, and the secondary α_s phase is constrained to grow in some special directions [30,31], thereby forming a slender structure; however, at room temperature, the β phase of the BCC structure possesses more slip systems, thus resulting in the generation of a secondary α_s phase with a smaller aspect ratio. At the same temperature, when the strain rate increases from 0.01 to 2000 s⁻¹, the aspect ratio of the

secondary α_s phase increases from 10:1 to 38:1. This phenomenon is likely attributable to the following two aspects. First, under high strain rate compression loading, only a part of the slip system inside the alloy can activate and respond quickly, especially in the α phase, where this limitation is more obvious due to the relatively stable HCP structure; therefore, the deformation is more concentrated on some special slip systems, resulting in a secondary α_s phase with a larger aspect ratio. Second, the stress is often concentrated in a special region of the material, and in the high stress region, the stress-induced phase transformation effect

(mainly manifested as the transformation from the β phase to the secondary α_s phase) of titanium alloys is more active [32], further promoting the formation of the elongated secondary α_s phase.

As mentioned in Section 3.1, the flow stress at low temperature is always higher than that at room temperature, which can be attributed to the low possibility of dislocation movement, high density of dislocations and twinning. In addition, the phase distribution also plays a critical role in the flow stress. As revealed in Fig. 12, a lower temperature corresponds to more α_p phase, which contributes more strength than β phase does, thus resulting in a higher flow stress.

Considering that the specimens do not fracture at 973–1173 K, it is also essential to characterize the microstructure. Specimens under four typical conditions, including (973 K, 0.01 s⁻¹), (973 K,

 1 s^{-1}), (1173 K, 0.01 s⁻¹) and (1173 K, 1 s^{-1}) were selected, and their microstructure is exhibited in Fig. 13. All the specimens still exhibit elongated bimodal microstructure; however, microstructure is closely related to the temperature and strain rate. Under the same strain rate conditions, the volume fraction of the α phase (primary α_p phase + secondary α_s phase) is inversely correlated with temperature. However, the relationship between the volume fraction of the α phase and the strain rate is dependent on the temperature. At 973 K ($\alpha+\beta$ phase region), a strain rate of 1 s⁻¹ corresponds to higher fractions of the α_p phase and α_s phase in comparison with the strain rate of 0.01 s⁻¹; thus a higher flow stress occurs, which agrees well with the trend shown in Fig. 6. At 1173 K, a strain rate of 1 s⁻¹ corresponds to a lower fraction of the α_p phase and a higher fraction of α_s phase. The different phase

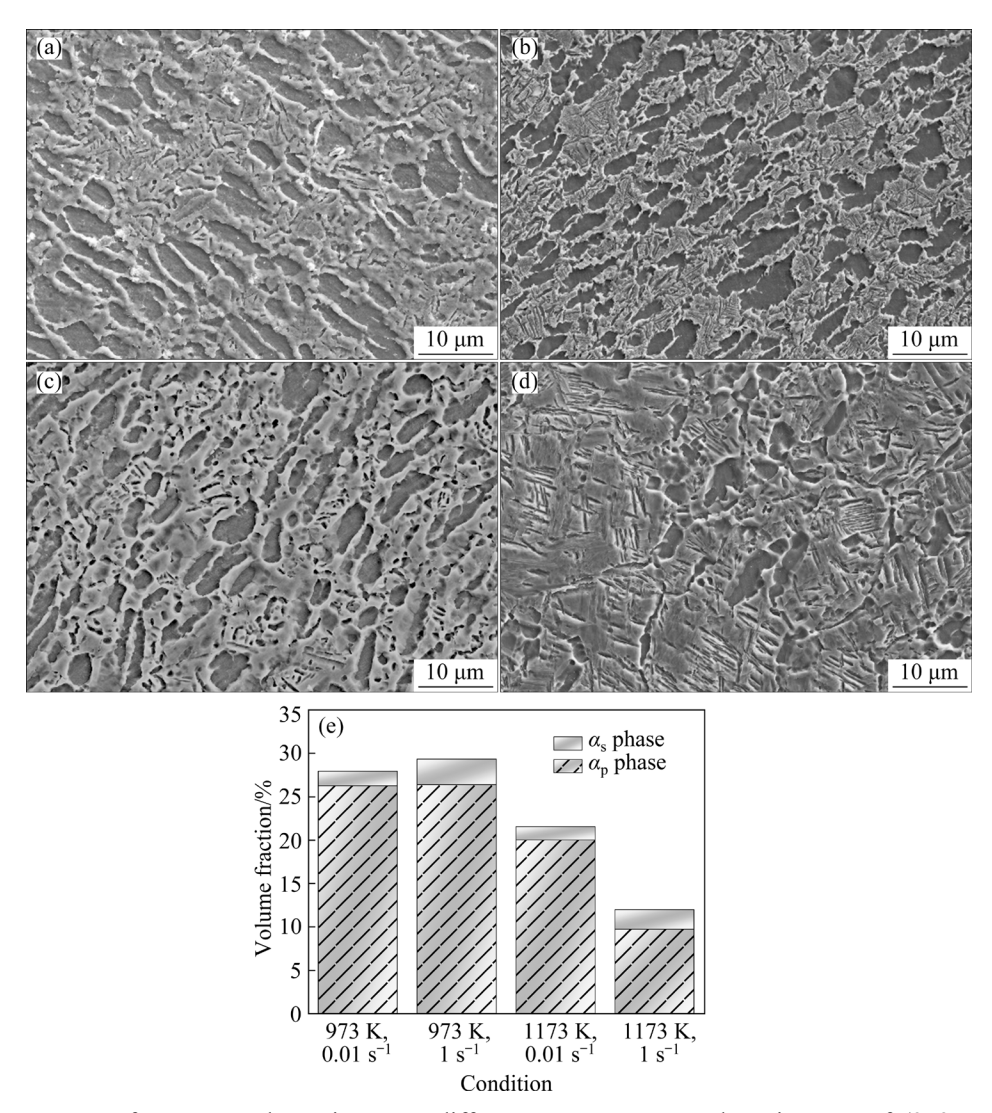


Fig. 13 Microstructure of compressed specimens at different temperatures and strain rates of (973 K, 0.01 s⁻¹) (a), (973 K, 1 s⁻¹) (b), (1173 K, 0.01 s⁻¹) (c) and (1173 K, 1 s⁻¹) (d); Statistics of α phase (e)

distributions under different extreme conditions are likely attributable to the comprehensive effect of temperature and strain rate that increasing temperature can inhibit the formation of α phases and increasing the strain rate can generate more α phases.

4 Constitutive behavior

The Johnson–Cook (JC) constitutive model is an empirical constitutive model that can describe the mechanical properties of materials over a wide strain, temperature, and strain rate range. Because of its concise structure and easy determination of parameters, it has become one of the most common material models in the engineering field [13]. The JC constitutive model is composed of three parts, namely, the strain hardening term, strain rate term and temperature softening term, and can be expressed as follows [33]:

$$\sigma = (A + B\varepsilon_{\rm pl}^{n}) \left[1 + C \ln \left(\frac{\dot{\varepsilon}}{\dot{\varepsilon}_{0}} \right) \right] \left[1 - \left(\frac{T - T_{\rm r}}{T_{\rm M} - T_{\rm r}} \right)^{s} \right]$$
 (6)

where A is the yield stress at the reference temperature and reference strain rate, B is the strain hardening coefficient, $\varepsilon_{\rm pl}$ is the true plastic strain, n is the strain hardening exponent, C is the strain rate hardening coefficient, $\dot{\varepsilon}_0$ is the reference strain rate, $T_{\rm r}$ is the reference temperature, $T_{\rm M}$ is the melting point of the material and s is the temperature softening coefficient. In the present study, the melting point of the $\alpha+\beta$ titanium alloy is 1543 K, as calculated by JMatpro software.

Figure 14 shows the relationship between the stress and temperature under different plastic strains. At 203-293 K, the flow stress of the titanium alloy is less affected by temperature and is mainly affected by strain hardening, which shows a synchronous increasing trend with the increase in strain. At 973-1173 K, the alloy has almost no strain hardening effect, and temperature softening effect is enhanced with increasing temperature, revealing obvious temperature sensitivity. There are significant differences in the strain hardening effect and temperature softening effect in the abovementioned two temperature ranges, which means that it is difficult to describe the mechanical behavior over a wide temperature range of 203-1173 K using the traditional JC constitutive model.

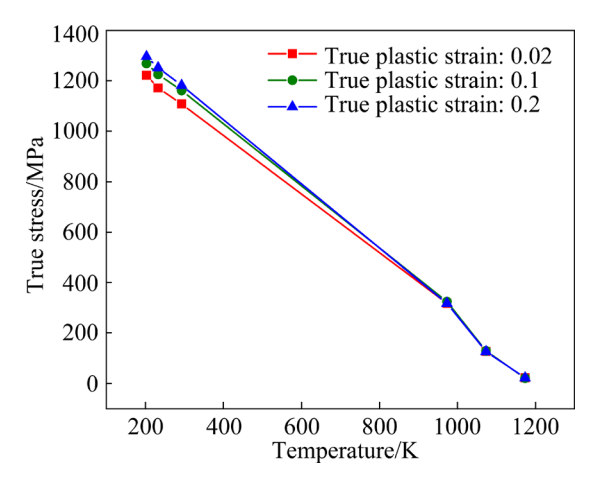


Fig. 14 True stress variation with temperature under different true plastic strain conditions for titanium alloys

Considering that accurately describing the deformation behavior of some materials is difficult with the traditional JC constitutive model, some researchers have revised the JC constitutive model. CAI et al [34] established a modified JC constitutive model by modifying the temperature softening term by considering the coupling effect of temperature, strain rate and strain softening phenomenon. This model can accurately predict the flow stress of an alloy in $\alpha + \beta$ phase region. ZHANG et al [35] described the temperature softening term through converting the temperature softening coefficient s to experimental temperaturedependent function s(T), and the calculation results strongly overlapped with the high temperature dynamic mechanical behavior of an AZ31 magnesium alloy. Therefore, this study uses the classical JC constitutive model to describe the strain hardening term and strain rate term, and a temperature softening coefficient s(T) is constructed to amend the temperature softening term. The revised JC constitutive model is as follows:

$$\begin{cases} \sigma = (A + B\varepsilon_{\rm pl}^{n}) \left[1 + C \ln \left(\frac{\dot{\varepsilon}}{\dot{\varepsilon}_{0}} \right) \right] \left[1 - \left(\frac{T - T_{\rm r}}{T_{\rm M} - T_{\rm r}} \right)^{s(T_{\rm e})} \right] \\ T = T_{\rm e} + \int_{0}^{\varepsilon_{\rm l}} \frac{\alpha}{\rho c_{p}} \sigma d\varepsilon_{\rm pl} \\ s(T_{\rm e}) = f(T_{\rm e}) \end{cases}$$
(7)

where ε_1 represents the axial plastic strain. T_e , α , ρ and c_p are the experimental temperature, heat conversion coefficient, material density and specific heat capacity, respectively. In the present study, α is

0.9; ρ equals 4550 kg/m³, as calculated by the Archimedes drainage method; c_p is 480 J/(kg·K), as calculated by the Jmatpro software.

The reference temperature (T_r) is 203 K, the reference strain rate $(\dot{\varepsilon}_0)$ is 0.01 s⁻¹, and the yield stress at the reference temperature and reference strain rate (A) is 1195 MPa. Based on the measured stress–strain data, the material constants of the JC model were calculated.

(1) Parameters n and B

When $\dot{\varepsilon} = \dot{\varepsilon}_0$ and $T = T_r$, Eq. (6) can be simplified to

$$\sigma = A + B\varepsilon_{\rm pl}^n \tag{8}$$

It can be converted to the following equation:

$$\ln(\sigma - A) = \ln B + n \ln \varepsilon_{\rm pl} \tag{9}$$

The values of n and B are 0.550 and 255 MPa, respectively, according to the linear fitting method, as illustrated in Fig. 15.

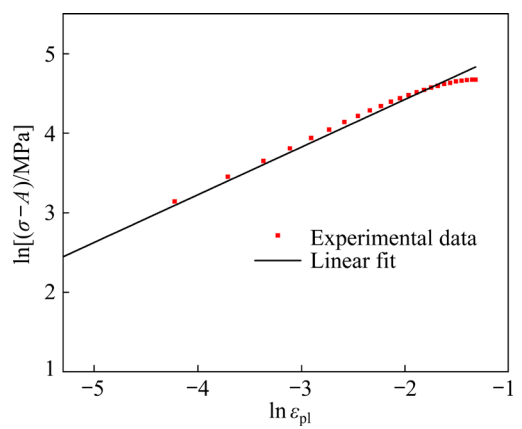


Fig. 15 Relationship between $\ln(\sigma - A)$ and $\ln \varepsilon_{\rm pl}$ (T=203 K, $\dot{\varepsilon}$ =0.01 s⁻¹)

(2) Parameter C

When $T=T_r$, Eq. (6) can be simplified to

$$\sigma = \left(A + B\varepsilon_{\rm pl}^{n}\right) \left[1 + C\ln\left(\frac{\dot{\varepsilon}}{\dot{\varepsilon}_{0}}\right)\right] \tag{10}$$

It can be converted to

$$C = \left(\frac{\sigma}{A + B\varepsilon_{\rm pl}^n} - 1\right) / \ln\left(\frac{\dot{\varepsilon}}{\dot{\varepsilon}_0}\right)$$
 (11)

The true stresses at yield under different strain rates (0.002, 0.005, 0.02, and 0.05 s⁻¹) at 203 K are used to obtain the corresponding C values, which are shown in Table 2. The C values under the different strain rate conditions are similar, and the average value is taken as 0.01625.

Table 2 C values of compressed specimens at different strain rates

Strain rate/s ⁻¹	0.002	0.005	0.02	0.05
С	0.01621	0.01622	0.01633	0.01624

(3) Parameter s(T)

When $\dot{\varepsilon} = \dot{\varepsilon}_0$, Eq. (6) can be simplified to

$$\sigma = (A + B\varepsilon_{\rm pl}^n) \left[1 - \left(\frac{T - T_{\rm r}}{T_{\rm M} - T_{\rm r}} \right)^{s(T_{\rm c})} \right]$$
 (12)

It can be converted to

$$s(T_{\rm e}) = \ln \left(1 - \frac{\sigma}{A + B\varepsilon_{\rm pl}^n} \right) / \ln \left(\frac{T - T_{\rm r}}{T_{\rm M} - T_{\rm r}} \right)$$
 (13)

The corresponding yield stresses at different temperatures (233, 293, 973, 1073 and 1173 K) under a strain rate of 0.01 s^{-1} are used to obtain the corresponding $s(T_e)$ values, which are given in Table 3.

Table 3 $s(T_e)$ values of compressed specimens at different temperatures

Temperatures/K	233	293	973	1073	1173
$s(T_{\rm e})$	-3.104	-2.331	-0.1227	-0.04661	-0.03012

Apparently, due to the significant differences in $s(T_e)$ under different temperature conditions, averaging those s values is unreasonable. Since $s(T_e)$ is affected by temperature, an expression needs to be created to describe $s(T_e)$ versus temperature, and the experimental temperatures T_e and $s(T_e)$ have a close relationship (Fig. 16) and can be fitted as follows:

$$s(T_e)=10947T_e^{-1.622}$$
 (14)

Based on the abovementioned results, the constitutive equation of the alloy is

$$\sigma = \begin{cases} (1195 + 255\varepsilon_{\rm pl}^{0.550})[1 + 0.0163\ln(\dot{\varepsilon}/\dot{\varepsilon}_{0})] \cdot \\ \left[1 - (\frac{T - T_{\rm r}}{T_{\rm M} - T_{\rm r}})^{s(T_{\rm e})}\right] \\ T = T_{\rm e} + \int_{0}^{\varepsilon_{\rm l}} \frac{\alpha}{\rho c_{p}} \sigma d\varepsilon_{\rm pl} \\ s(T_{\rm e}) = 10947T_{\rm e}^{-1.622} \end{cases}$$

$$(15)$$

To verify the modified JC model, several representative true plastic stress—true strain curves obtained from the model are compared with the

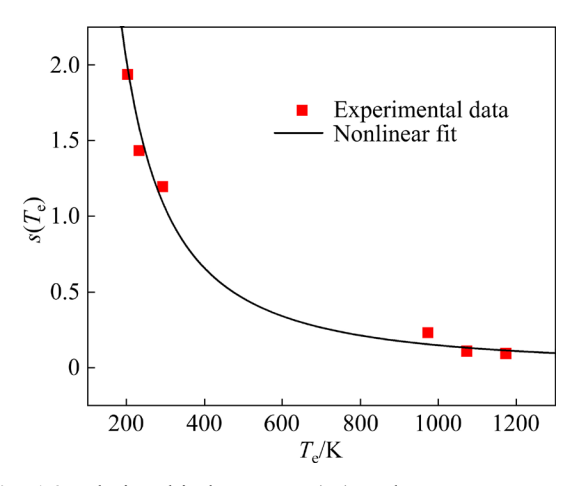


Fig. 16 Relationship between $s(T_e)$ and T_e

experimental true stress—strain curves, as shown in Fig. 17. Clearly, the difference between the experimental data and calculated data at 203–1173 K is relatively small, confirming the reliability of the constitutive model.

To further quantitatively describe the prediction accuracy of modified JC constitutive model, three important indexes including the correlation coefficient (R^2), root mean square error (RMSE) and average absolute relative error (AARE)

are introduced [36].

The R^2 value is a general fit of measure from a predicted regression curve to the original set of data on a scale from 0 (worst) to 1 (perfect), and it can be described as follows [36]:

$$R^{2}=1-\frac{\sum_{i=1}^{n}\left(\sigma_{p}-\sigma_{e}\right)^{2}}{\sum_{i=1}^{n}\left(\sigma_{p}-\overline{\sigma}_{e}\right)^{2}}$$
(16)

where σ_p , σ_e and $\overline{\sigma}_e$ represent predicted true stress, experimental true stress and average experimental true stress, respectively.

The RMSE is the mean square difference between the predicted data and measured data, and can be expressed as [36]

$$RMSE = \sqrt{\frac{1}{N} \sum_{i=1}^{N} \left(\sigma_{p} - \sigma_{e}\right)^{2}}$$
 (17)

The AARE is used to evaluate the relative error between the predicted data and measured data. The equation for AARE is [37]

$$ARRE = \frac{1}{N} \sum_{i=1}^{N} \left| \frac{\sigma_{e} - \sigma_{p}}{\sigma_{e}} \right| \times 100\%$$
 (18)

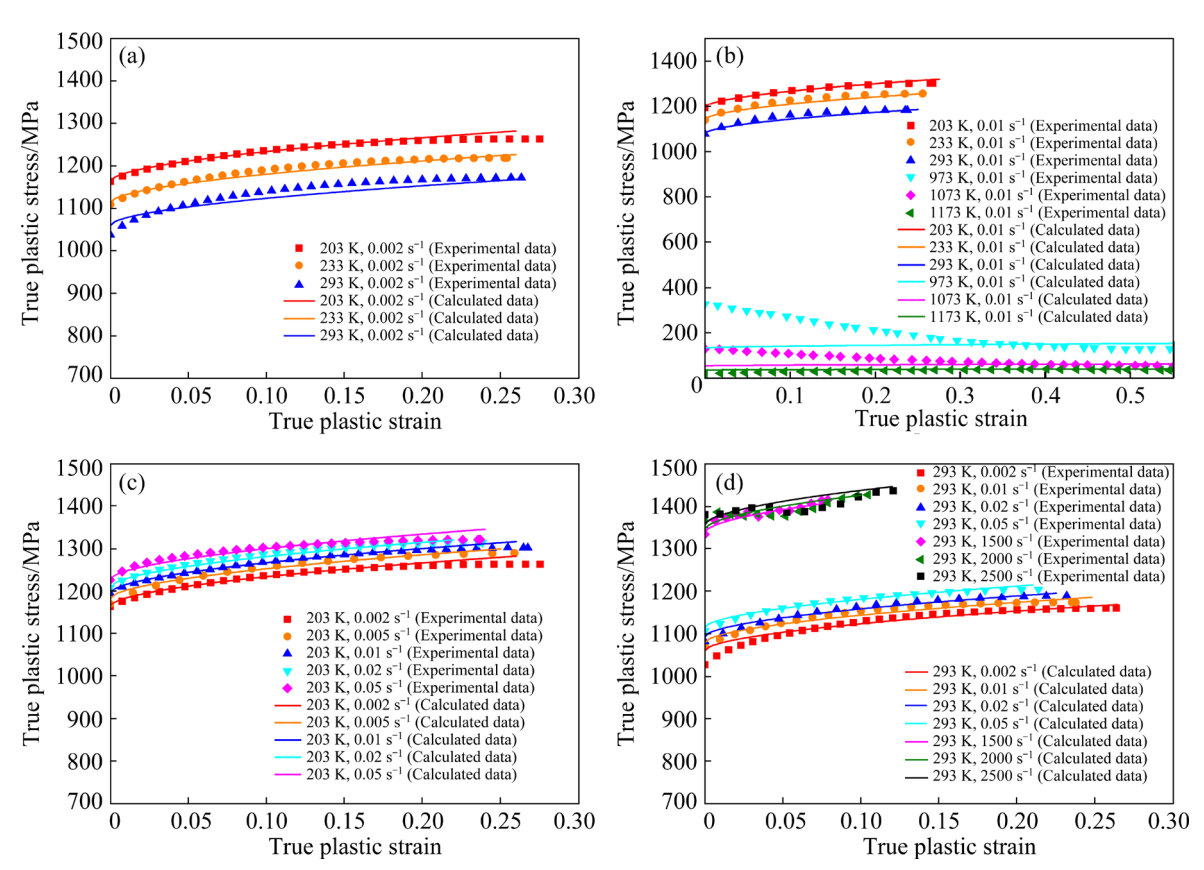


Fig. 17 Comparison between calculated data and experimental data of true plastic stress–strain curves under different conditions: (a) $0.002 \, \mathrm{s}^{-1}$, $203-293 \, \mathrm{K}$; (b) $0.01 \, \mathrm{s}^{-1}$, $203-1173 \, \mathrm{K}$; (c) $203 \, \mathrm{K}$, $0.002-0.05 \, \mathrm{s}^{-1}$; (d) $293 \, \mathrm{K}$, $0.002-2500 \, \mathrm{s}^{-1}$

On the basis of the experimental results and Eqs. (16)–(18), R^2 , RMSE and ARRE can be calculated and are summarized in Table 4. The predicted results are highly consistent with the experimental results under low strain rate predicted conditions. However, the results somewhat deviate from the experimental results under high strain rate conditions (exceeding 1500 s⁻¹). Generally, this modified JC constitutive model is reliable and can ensure the accuracy of the numerical calculation.

Experimental condition	R^2	RMSE	AARE
203 K, 0.002 s ⁻¹	0.9606	7.5333	0.0040
$233 \text{ K}, 0.002 \text{ s}^{-1}$	0.9661	7.0991	0.0053
$293~K,0.002~s^{-1}$	0.9539	13.7908	0.0111
$203 \text{ K}, 0.01 \text{ s}^{-1}$	0.9812	4.9897	0.0026
$233 \text{ K}, 0.01 \text{ s}^{-1}$	0.9698	11.6695	0.0085
$293 \text{ K}, 0.01 \text{ s}^{-1}$	0.9520	13.1459	0.0101
$973 \text{ K}, 0.01 \text{ s}^{-1}$	0.9653	58.5255	0.2571
$1073 \text{ K}, 0.01 \text{ s}^{-1}$	0.9870	30.9238	0.2535
1173 K, 0.01 s ⁻¹	0.9718	7.5927	0.2182
$203 \; \mathrm{K}, 0.005 \; \mathrm{s}^{-1}$	0.9704	5.5936	0.0036
$203 \text{ K}, 0.02 \text{ s}^{-1}$	0.9777	4.8361	0.0033
$203 \text{ K}, 0.05 \text{ s}^{-1}$	0.9470	9.3350	0.0057
$293 \text{ K}, 0.02 \text{ s}^{-1}$	0.9675	5.8661	0.0042
$293 \text{ K}, 0.05 \text{ s}^{-1}$	0.9699	21.2437	0.0176
$293 \text{ K}, 1500 \text{ s}^{-1}$	0.8691	6.9108	0.0044
$293 \text{ K}, 2000 \text{ s}^{-1}$	0.8214	13.4232	0.0088
$293 \text{ K}, 2500 \text{ s}^{-1}$	0.8091	15.0016	0.0110

5 Conclusions

- (1) Ti-5.7Al-2.9Nb-1.8Fe-1.6Mo-1.5V-1Zr alloy exhibits a positive strain rate sensitivity under different temperature conditions. At room temperature and low temperature, the strain rate sensitivity is weak under a narrow range of strain rates; at high temperature, the strain rate sensitivity is strong, and the flow stress significantly increases with increasing strain rate.
- (2) Ti-5.7Al-2.9Nb-1.8Fe-1.6Mo-1.5V-1Zr alloy exhibits significant negative temperature sensitivity under different strain rate conditions. At

low temperature and room temperature, the alloy possesses weak temperature sensitivity; at high temperature, the alloy exhibits much stronger temperature sensitivity than that at low temperature and room temperature.

- (3) Ti-5.7Al-2.9Nb-1.8Fe-1.6Mo-1.5V-1Zr alloy reveals typical shear fracture failure, which is somewhat influenced by the temperature and strain rate. As the compression temperature increases, the fracture morphology transforms from a shallow "fish scale" structure to dimples; as the strain rate increases, flat and smooth areas and a small amount of ductile dimples appear on the fracture surface.
- (4) The deformed microstructure is closely related to the temperature and strain rate. At low temperature and room temperature, the volume fraction and size of the primary α_p phase are negatively correlated with the temperature and strain rate, and a high strain rate is beneficial for increasing the aspect ratio of the α_s phase. At high temperatures, the volume fraction of α phase is inversely correlated with temperature.
- (5) Based on the experimental results, a modified Johnson–Cook constitutive model of the $\alpha+\beta$ titanium alloy is established. The parameter $s(T_e)$ is expressed as a function related to the temperature. The calculation results of the constitutive model agree well with the experimental data.

CRediT authorship contribution statement

Wen-fei PENG: Conceptualization, Investigation, Formal analysis, Writing – Original draft, Writing – Review & editing; Chao-qi DONG: Conceptualization, Methodology, Writing – Review & editing, Formal analysis; Qiao-dong HUANG: Investigation, Resources, Validation; Xiao-feng WANG: Methodology, Formal analysis, Writing – Review & editing, Supervision; Oleksandr MOLIAR: Formal analysis, Writing – Review & editing.

Declaration of competing interest

The authors declare that they have no known competing financial interests or personal relationships that could have appeared to influence the work reported in this paper.

Acknowledgments

This work was supported by the National Natural Science Foundation of China (Nos. 11972202, 52075272), the Major Project of Ningbo Science and

Technology Innovation, China (Nos. 2021Z099, 2023Z005), National Key Laboratory of Shock Wave and Detonation Physics, China (No. JCKYS2023212005), State Key Laboratory for Advanced Metals and Materials, China (No. 2023-Z04), Zhejiang Provincial Natural Science Foundation, China (No. LMS25E050015) and the K. C. Wong Magna Fund from Ningbo University, China.

References

- [1] SHI X H, ZHANG Q, JING Z, FAN Z Y, LIU J L, QIAO J W. Strengthening behavior and model of ultra-high strength Ti-15Mo-2.7Nb-3Al-0.2Si titanium alloy [J]. Transactions of Nonferrous Metals Society of China, 2024, 34: 1136-1149.
- [2] QIU Guan-zhou, GUO Yu-feng. Current situation and development trend of titanium metal industry in China [J]. International Journal of Minerals Metallurgy and Materials, 2022, 29: 599–610.
- [3] HAAR G M T, BECKER T H. The influence of microstructural texture and prior beta grain recrystallisation on the deformation behaviour of laser powder bed fusion produced Ti-6Al-4V [J]. Materials Science and Engineering A, 2021, 814: 141185.
- [4] WANG Ke, YAN Zhi-bing, ZHOU Yu, WEI Shi-zhong, WANG Xiao-dong, XIN Ren-long, LIU Qing. Slip initiation in interlayered β and corresponding slip transfer during compression of a lamellar-structure titanium alloy [J]. Results in Physics, 2020, 18: 103276.
- [5] GUO Ping, ZHAO Yong-qing, ZENG Wei-dong, HONG Quan. The effect of microstructure on the mechanical properties of TC4-DT titanium alloys [J]. Materials Science and Engineering A, 2013, 563: 106–111.
- [6] SHI Zhi-feng, GUO Hong-zhen, LIU Rui, WANG Xiao-chen, YAO Ze-kun. Microstructure and mechanical properties of TC21 titanium alloy by near-isothermal forging [J]. Transactions of Nonferrous Metals Society of China, 2015, 25: 72-79.
- [7] YU Jia-shi, ZHAO Qin-yang, HUANG Shi-xing, ZHAO Yong-qing, LU Jin-wei, DONG Long-long, TIAN Ning. Enhanced mechanical and tribological properties of graphene nanoplates reinforced TC21 composites using spark plasma sintering [J]. Journal of Alloys and Compounds, 2021, 873: 159764.
- [8] ZHANG Tian-long, ZHU Jia-ming, YANG Tao, LUAN Jun-hua, KONG Hao-jie, LIU Wei-hong, CAO Bo-xuan, WU Shi-wei, WANG Dong, WANG Yun-zhi, LIU Chain-Tsuan. A new α+β Ti-alloy with refined microstructures and enhanced mechanical properties in the as-cast state [J]. Scripta Materialia, 2022, 207: 114260.
- [9] GUO Kai, MENG Kang, MIAO Dun, WANG Qing-feng, ZHANG Chuan-you, WANG Tian-sheng. Effect of annealing on microstructure and tensile properties of skew hot rolled Ti-6Al-3Nb-2Zr-1Mo alloy tube [J]. Materials Science and Engineering A, 2019, 766: 138346.
- [10] ZHU Qiang-qiang, YANG Xing-di, LAN Hui-fang, WANG Dong-xiao, LOU Hong-tao, LI Jian-ping. Effect of solution

- treatments on microstructure and mechanical properties of Ti-6Al-4V alloy hot rolled sheet [J]. Journal of Materials Research and Technology 2023, 23: 5760–5771.
- [11] GUO Bao-qi, JONAS J J. Dynamic transformation during the high temperature deformation of titanium alloys [J]. Journal of Alloys and Compounds, 2021, 884: 161179.
- [12] LIU Gao-feng, ZHANG Shang-zhou, CHEN Li-qing, QIU Jian-xun. Deformation behavior and microstructural evolution during hot compression of an α+β Ti-6.5Al-3.5Mo-1.5Zr-0.3Si alloy [J]. International Journal of Minerals Metallurgy and Materials, 2011, 18: 344-351.
- [13] ZHANG Chang-ming, MU A, WANG Yun, ZHANG Hui. Study on dynamic mechanical properties and constitutive model construction of TC18 titanium alloy [J]. Metals, 2019, 10: 44.
- [14] ZHENG Chao, WANG Fu-chi, CHENG Xin-wang, LIU Jin-xu, LIU Teng-teng, ZHU Zheng-xin, YANG Xia-wen, PENG Mei-qi, JIN Dan. Capturing of the propagating processes of adiabatic shear band in Ti-6Al-4V alloys under dynamic compression [J]. Materials Science and Engineering A, 2016, 658: 60-67.
- [15] LEI Li-ming, HUANG Xu, WANG Min-min, WANG Li-qiang, QIN Ji-ning, LU Shi-qiang. Effect of temperature on deformation behavior and microstructures of TC11 titanium alloy [J]. Materials Science and Engineering A, 2011, 528: 8236–8243.
- [16] YU Yang-bo, YAN Hong-ge, CHEN Ji-hua, XIA Wei-jun, SU Bin, DING Tian, LI Zen-zhen, SONG Min. Flow behavior and dynamic transformation of bimodal TC17 titanium alloy during high strain rate hot compression [J]. Journal of Alloys and Compounds, 2022, 912: 165260.
- [17] LEE W S, CHEN T H, HUANG S C. Impact deformation behaviour of Ti-6Al-4V alloy in the low-temperature regime [J]. Journal of Nuclear Materials 2010, 402: 1-7.
- [18] SINGH G, BAJARGAN G, DATTA R, RAMAMURTY U. Deformation and strength of Ti-6Al-4V alloyed with B at cryogenic temperatures [J]. Materials Science and Engineering A, 2014, 611: 45-57.
- [19] SEMENOVA I P, MODINA J, POLYAKOV A V, KLEVTSOV G V, KLEVTSOVA N A, PIGALEVA I N, VALIEV R Z. Charpy absorbed energy of ultrafine-grained Ti-6Al-4V alloy at cryogenic and elevated temperatures [J]. Materials Science and Engineering A, 2019, 743: 581-589.
- [20] WANG Q, REN J Q, ZHANG B B, XIN C, WU Y K, ZHANG L. Simultaneously improved strength and elongation at cryogenic temperature in Ti-5Al-1V-1Sn-1Zr-0.8Mo alloy with a bimodal structure [J]. Materials Science and Engineering A, 2021, 824: 141792.
- [21] CHENG Fang, WANG Hua-ming, LI Zhuo, CHENG Xu, ZHENG Dong-dong, ZHANG shu-quan, HU Xu, ZHANG Hao, LIU Min. Dynamic compression deformation behavior of laser directed energy deposited α+β duplex titanium alloy with basket-weave morphology [J]. Additive Manufacturing, 2023, 61: 103336.
- [22] ZHU Yan-chun, FAN Jia-xin, LI Zi-liang, LUO Yuan-yuan, NIU Yong. Study of strain rate sensitivity exponent and strain hardening exponent of typical titanium alloys [J]. Materials Today Communications, 2022, 30: 103060.
- [23] YIN Liang-wei, UMEZAWA O. Crystal plasticity analysis of

- temperature-sensitive dwell fatigue in Ti-6Al-4V titanium alloy for an aero-engine fan disc [J]. International Journal of Fatigue, 2022, 156: 106688.
- [24] ZHAO Y T, LI X W, FANG W B. Microstructure and mechanical properties of TC4 titanium alloy at the temperature of 77 K [J]. Metals, 2023, 13: 1086.
- [25] LYU Z Y, FAN X S, LEE C, WANG S Y, FENG R, LIAW P K. Fundamental understanding of mechanical behavior of high-entropy alloys at low temperatures: A review [J]. Journal of Materials Research, 2018, 33: 2998–3010.
- [26] LIU Yan-hui, NING Yong-quan, YANG Xue-mei, YAO Ze-kun, GUO Hong-zhen. Effect of temperature and strain rate on the workability of FGH4096 superalloy in hot deformation [J]. Materials & Design, 2016, 95: 669–676.
- [27] ZAFARI A, XIA K N. Stress induced martensitic transformation in metastable β Ti-5Al-5Mo-5V-3Cr alloy: Triggering stress and interaction with deformation bands [J]. Materials Science and Engineering A, 2018, 724: 75–79.
- [28] CHEN Kai, FAN Qun-bo, YAO Jia-hao, YANG Lin, XU Shun, GAO Yu, LEI Wei. Influence of stress-induced α" phase transformation on mechanical properties in metastable β type Ti-5Al-2.5Cr-5Mo-1Sn alloy [J]. Journal of Alloys and Compounds, 2022, 920: 165563.
- [29] MENG M, FAN X G, YANG H, GUO L G, ZHAN M, GAO P F. Precipitation of secondary alpha in competition with epitaxial growth of primary alpha in two-phase titanium alloys [J]. Journal of Alloys and Compounds, 2017, 714: 294–302.
- [30] XU Y L, JOSEPH S, KARAMCHED P, FOX K, RUGG D, DUNNE F P E, DYE D. Predicting dwell fatigue life in titanium alloys using modelling and experiment [J].Nature Communications, 2020, 11: 5868.
- [31] ZHANG Hao, OU Xiao-qin, WEI Bin-qiang, NI Song, SONG Min. Strain direction dependency of deformation

- mechanisms in an HCP-Ti crystalline by molecular dynamics simulations [J]. Computational Materials Science, 2020, 172: 109328.
- [32] BHATTACHARJEE A, BHARGAVA S, VARMA V K, KAMAT S V, GOGIA A K. Effect of β grain size on stress induced martensitic transformation in β solution treated Ti-10V-2Fe-3Al alloy [J]. Scripta Materialia, 2005, 53: 195–200.
- [33] ZHAO Yan-hua, SUN Jie, LI Jian-feng, YAN Yu-qin, WANG Ping. A comparative study on Johnson-Cook and modified Johnson-Cook constitutive material model to predict the dynamic behavior laser additive manufacturing FeCr alloy [J]. Journal of Alloys and Compounds, 2017, 723: 179–187.
- [34] CAI Jun, WANG Kuai-she, ZHAI Peng, LI Fu-guo, YANG Jie. A modified Johnson-Cook constitutive equation to predict hot deformation behavior of Ti-6Al-4V alloy [J]. Journal of Materials Engineering and Performance, 2014, 24: 32-44.
- [35] ZHANG Feng, LIU Zheng, WANG Yue, MAO Ping-li, KUANG Xin-wen, ZHANG Zheng-lai, JU Ying-dong, XU Xiao-zhong. The modified temperature term on Johnson—Cook constitutive model of AZ31 magnesium alloy with {0002} texture [J]. Journal of Magnesium and Alloys, 2020, 8: 172–183.
- [36] MCELFRESH C, ROBERTS C, HE S, PRIKHODKO S, MARIAN J. Using machine-learning to understand complex microstructural effects on the mechanical behavior of Ti-6Al-4V alloys [J]. Computational Materials Science, 2022, 208: 111267.
- [37] TRIMBLE D, O'DONNELL G E. Flow stress prediction for hot deformation processing of 2024Al-T3 alloy [J]. Transactions of Nonferrous Metals Society of China, 2016, 26: 1232-1250.

Ti-5.7Al-2.9Nb-1.8Fe-1.6Mo-1.5V-1Zr 合金在极端条件下的压缩力学行为及显微组织演变

彭文飞¹, 董超琪¹, 黄巧东¹, 汪小锋^{1,2}, Oleksandr MOLIAR¹

- 1. 宁波大学 机械工程与力学学院, 宁波 315211;
- 2. 宁波大学 冲击与安全工程教育部重点实验室, 宁波 315211

摘 要:系统研究了 Ti-5.7Al-2.9Nb-1.8Fe-1.6Mo-1.5V-1Zr 合金在极端条件下的力学行为与显微组织演变。结果表明,应变速率和温度对力学行为和显微组织均有显著影响。合金在所有温度和应变速率条件下均表现出正应变速率敏感性和负温度敏感性。合金在热轧状态下为典型的双态组织,包括等轴初生 α_p 相与转变 β 相。压缩变形后,变形双态组织特征极大依赖于温度和应变速率。在低温和室温条件下, α_p 相的体积分数和尺寸与温度和应变速率负相关;在高温条件下, α 相的体积分数与温度负相关。建立了修正 Johnson-Cook 本构模型,预测结果与实验结果吻合较好。

关键词: 钛合金; 极端条件; 力学行为; 显微组织; 修正 Johnson-Cook 本构模型

(Edited by Bing YANG)